AIAA 81-1202R

# Supersonic Nonlinear Potential Flow with Implicit Isentropic Shock Fitting

Michael J. Siclari*
*Grumman Aerospace Corporation, Bethpage, N. Y.*

**A fully implicit nonconservative marching technique is utilized to solve the full potential flow equation in a spherical coordinate frame for supersonic inviscid flow. Transonic techniques form the basis for the numerical scheme in the cross flow plane which allows for capture of both bow and embedded shocks. A column relaxation scheme is presented which exhibits enhanced computational efficiency over ring relaxation schemes. An implicit bow shock fitting procedure satisfying the isentropic jump condition is also presented and compared to the shock capture method, shock fit Euler solutions, and experimental data for arbitrary conical surfaces.**

## Nomenclature

$R_s$ = numerical residual of bow shock jump condition
$R_\phi$ = numerical residual of full potential equation
$\alpha$ = angle of attack
$\delta$ = semi-minor axis angle of elliptic cone
$\theta_c$ = semi-major axis angle of elliptic cone

## Introduction

THE aerodynamic designer of supersonic wings relies heavily on linear theory methods at low lift coefficients and ultimately on wind-tunnel data. The failure of linearized theory in supercritical cross flow regions is fairly well known.[1-6,8,9] Hence, in the realm of high lift coefficients, where supercritical cross flow regimes are likely to occur, other analytical methods must be sought if the aerodynamicist is to achieve his design goals in a cost efficient manner.

Nonlinear methods can predict the formation of supercritical regions and cross flow shocks.[2-9,11] An efficient nonlinear methodology can offer the design engineer a valuable tool in that he can tailor a wing to optimize supercritical lift and minimize the strength of cross flow shocks, thus reducing cross flow shock drag, and the possibility of shock induced boundary-layer separation.

Nonlinear methods that solve the Euler equations using an explicit marching technique[2-5] have been found to be efficient tools in the high supersonic to hypersonic Mach number regime. In the low to moderate supersonic range ($1.1 \leq M_\infty \leq 2.0$) these methods inherently become computationally inefficient for wing planforms that have sweep angles less than 70 deg because the Courant-Friedrichs-Lewy (CFL) condition for stability reduces the axial marching step size to zero as the axial Mach number approaches unity. Other difficulties are resolution of vortical layers, time consuming starting solutions,[5] and inability to capture embedded and bow shocks.

In Ref. 8, an implicit numerical technique was developed to solve the full potential equation in nonconservation form for conical flows in a spherical coordinate system readily adaptable to supersonic flows. The assumption of conical similitude reduces the full potential equation to an equation in the spherical cross flow plane that closely resembles the two-dimensional transonic full potential equation. The potential equation is solved in a conformally mapped cross flow plane ($r$ = const) using the type dependent mixed flow relaxation techniques and rotated difference scheme formulated by Jameson.[10] The bow and embedded cross flow shocks are captured using a supersonic cross flow switching criterion. A "ring" relaxation technique is employed sweeping from an arbitrary finite outer boundary of freestream conditions (i.e., zero reduced potential) through the bow shock down to the body surface. The use of a spherical coordinate system ameliorates the axial Mach number problem allowing the computation of flows at much lower Mach numbers. This technique was found to be highly accurate when compared to Euler solutions and experiments at moderate Mach numbers. As a result the technique was used in Ref. 7 to tailor the design of a high lift supercritical conically cambered wing with a shockless recompression at design conditions. The experiments confirmed the accuracy of the numerical results.

The success of the nonlinear conical flow methodology led to extending these techniques to three-dimensional flows. This task was initiated for delta wing geometries.[9,11] A fully implicit marching technique was utilized where the additional three-dimensional or nonconical terms were treated as forcing functions in the numerical formulation. The nonconical terms lead to a more complex governing equation and, in general, due to the cross flow plane conformal mappings, a nonorthogonal mesh. Satisfactory results were obtained for delta wings with subsonic leading edges when compared to Euler solutions and experiment. Excellent results were also obtained for axisymmetric bodies of revolution at zero angle of attack when the outer mesh boundary was conformed to the body simulating the general behavior of the bow shock.

This technique was found to be satisfactory for nonconical flows as long as the cross flow criteria for switching and, hence, shock capturing, remained a reasonably valid approximation (e.g., delta wings). Typical geometries that violate this criteria are variable sweep wings and wing-body combinations that depart radically from the initial conical flow and bow shock formed at the apex. In these cases, the accuracy of the bow shock capture technique can be expected to diminish leading to serious errors in the surface pressures. The nonconservation form of the governing equation also leads to questions about the accuracy of the capture technique as the shock strength increases. A more desirable procedure would be to fit the bow shock using an appropriate isentropic jump condition.

In this study, the general nonconical numerical formulation will be re-evaluated on the basis of computational efficiency. A more efficient "column" relaxation technique is presented and compared to the "ring" relaxation method of Ref. 8 for conical flows. A fully implicit conical bow shock fitting technique is presented and compared with the captured solutions of the column successive line over relaxation (SLOR) method.

Presented as Paper 81-1202 at the AIAA 14th Fluid and Plasma Dynamics Conference, Palo Alto, Calif., June 23-25, 1981; submitted July 20, 1981; revision received Nov. 13, 1981. 

*Staff Scientist, Research Department. Member AIAA.

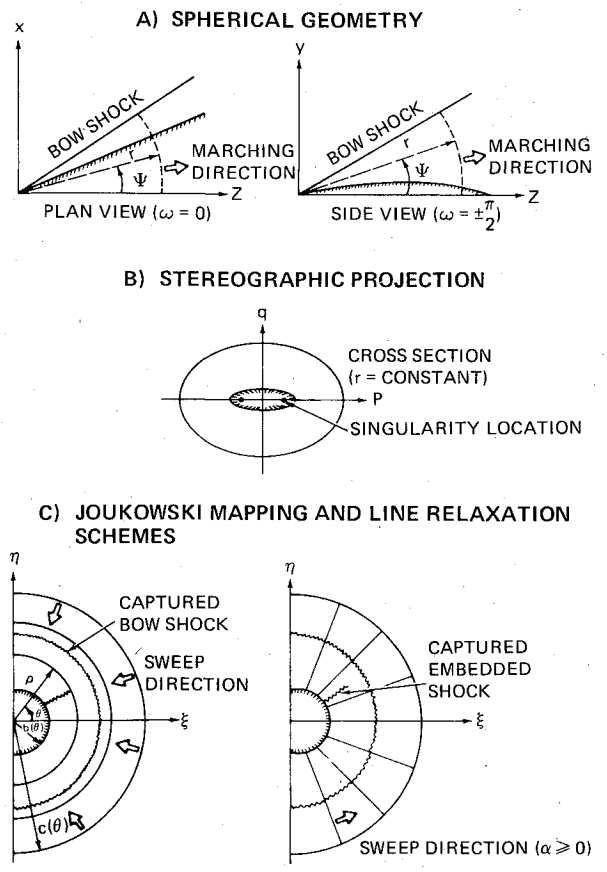


**Fig. 1 Coordinate transformations and relaxation techniques.**

For completeness, a brief review of the mappings and grid generation, governing equation, and velocity definitions of Refs. 8 and 9 will follow in the next two sections.

## Mappings and Grid Generation

A series of coordinate transformations are utilized to generate a coordinate mesh in the physical domain that is capable of resolving the large gradients that usually arise near wing leading edges in the cross flow plane. Figure 1 illustrates the sequence of mappings. The governing inviscid irrotational equation is written in a spherical coordinate system $(r,\omega,\psi)$ defined by

$$x=r\cos\omega\sin\psi \qquad y=r\sin\omega\sin\psi \qquad z=r\cos\psi \tag{1}$$

A sterographic projection is then applied to the cross-sectional coordinates on the surface of a sphere $r=\text{const}$.

$$p+iq=\tan\left(\frac{\psi}{2}\right)e^{i\omega} \tag{2}$$

A Joukowski mapping of the form

$$\frac{S-S_0(r)}{S+\bar{S}_0(r)}=\left(\frac{\Gamma-S_0(r)}{\Gamma+\bar{S}_0(r)}\right) \tag{3}$$

where $\Gamma=\rho e^{i\theta}$ and $S=p+iq$ is then utilized to transform the cross-sectional coordinates $(p,q,r)$ to a near circle $(\rho,\theta,R)$. A further shearing transformation is applied to the mapped domain to generate a computational grid

$$X=\theta \qquad Y=\frac{\rho-b(\theta,R)}{C(\theta,R)-b(\theta,R)} \qquad Z=R \tag{4}$$

where $b$ is a coordinate line representing the cross-sectional surface and $C$ a finite outer boundary. In the bow shock capture technique (BSC), $C$ will be a somewhat arbitrarily prescribed but continuous outer boundary of freestream conditions (i.e., $C$ must lie outside the bow shock). If the bow shock is fit (BSF), $C$ will then be the bow shock surface as will be demonstrated in a later section.

The complication that arises in three-dimensional flow is the dependence of the singularity location $S_0$ on $r$. This dependence, in general, will cause the mapped coordinates to be nonorthogonal. The nonorthogonality in three dimensions generates a fairly complex governing equation which is tedious to derive (see Ref. 9). The nonorthogonality occurs for geometries of varying cross-sectional shape that require an axial $(Z)$ variation of the singularity location.

In addition to a metric $H$ of the two mappings, the nonorthogonality leads to radial mesh derivatives denoted by $h_1$ and $h_2$, or

$$H(\rho,\theta,R)\equiv\frac{\sin\psi}{(p^2+q^2)^{1/2}}h$$

$$h_1(\rho,\theta,R)\equiv\frac{\partial\rho}{\partial r} \qquad h_2(\rho,\theta,R)\equiv\frac{1}{\rho}\frac{\partial\theta}{\partial r} \tag{5}$$

where $h=|\partial S/\partial\Gamma|$.

## Governing Equation and Velocity Definitions

The inviscid governing equation can be written in terms of the velocity vector $Q$ and the speed of sound $a$, as

$$a^2\nabla\cdot\boldsymbol{Q}-\tfrac{1}{2}\boldsymbol{Q}\cdot\nabla(\boldsymbol{Q}\cdot\boldsymbol{Q})=0 \tag{6a}$$

and

$$a^2+\frac{\gamma-1}{2}\boldsymbol{Q}\cdot\boldsymbol{Q}=a_0^2 \tag{6b}$$

The assumption of irrotationality is introduced through a perturbation potential of the form

$$\boldsymbol{Q}=\boldsymbol{q}+\boldsymbol{q}_\infty=\nabla\varphi+\boldsymbol{q}_\infty$$

where

$$\varphi\equiv RF(\rho,\theta,R)$$

$$\nabla\varphi\equiv u\boldsymbol{i}_\theta+v\boldsymbol{i}_\rho+w\boldsymbol{i}_r=\frac{1}{\rho RH}\varphi_\theta\boldsymbol{i}_\theta+\frac{1}{RH}\varphi_\rho\boldsymbol{i}_\rho+\varphi_r\boldsymbol{i}_r \tag{7}$$

The velocity vector $Q$ is defined as

$$\boldsymbol{Q}\equiv U\boldsymbol{i}_\theta+V\boldsymbol{i}_\rho+W\boldsymbol{i}_r$$

where

$$U=u+u_\infty=\frac{1}{\rho H}\frac{\partial F}{\partial\theta}+u_\infty(\rho,\theta,R)$$

$$V=v+v_\infty=\frac{1}{H}\frac{\partial F}{\partial\rho}+v_\infty(\rho,\theta,R)$$

$$W=w+w_\infty=F+R\frac{\partial F}{\partial r}+w_\infty(\rho,\theta,R) \tag{8}$$

For conical flow, the coordinates are orthogonal and the governing nonconservative equation can be written in the

mapped coordinates as

$$\frac{(a^2-U^2)}{\rho^2}F_{\theta\theta}-\frac{2}{\rho}UVF_{\rho\theta}+(a^2-V^2)F_{\rho\rho}+\frac{2}{\rho^2}UVF_{\theta}$$
$$+\frac{(a^2-U^2)}{\rho}F_{\rho}+H^2F(2a^2-V^2-U^2)$$
$$+f(U,V,H,H_{\rho},H_{\theta})=0 \tag{9}$$

where $H$ is the metric associated with the mappings. Equation (9) has the same characteristic form as the two-dimensional transonic nonconservation form of the full potential flow equation and can be solved numerically in a similar fashion. The basic numerics are essentially those developed by Jameson[10] which utilizes a rotated difference scheme. If the shearing transformation Eq. (4) is applied to Eq. (9), the following general form is obtained for the governing equation in the computational domain:

$$A_1F_{xx}+A_2F_{xy}+A_3F_{yy}+A_4F_x+A_5F_y+A_6F+A_7=0 \tag{10}$$

Jameson's rotated difference scheme is applied to the principal part of Eq. (10) when the local cross flow ($Q_c^2=U^2+V^2$) is supersonic, where it can be shown that

$$A_1F_{xx}+A_2F_{xy}+A_3F_{yy}=(a^2-Q_c^2)F_{ss}+a^2F_{nn} \tag{11}$$

The terms and coefficients of Eqs. (9-11) can be found in Ref. 8.

For general three-dimensional flow, the governing equation in the computational domain can be written as

$$(A_1-B_1)F_{xx}+(A_2-B_2)F_{xy}+(A_3-B_3)F_{yy}$$
$$+(A_4-B_4)F_y+A_5F_x+A_6w+(A_7-B_7)$$
$$=B_8F_{zz}+B_9F_{xz}+B_{10}F_{yz}+B_{11}F_z \tag{12}$$

where the coefficients $A_i$ are identical to the conical terms defined in Ref. 8, and the $B_i$ coefficients represent the nonconical terms defined in Ref. 9. The $B_i$ coefficients all contain an $r$ dependence that vanishes identically in conical flow reducing Eq. (12) to the conical Eq. (9). In the actual three-dimensional computation, all flows are initiated at $r=0$ with a conical solution of Eq. (9) using the cross-sectional coordinates at $r=r+\Delta r$. As a result, the three-dimensional computation is easily initiated utilizing the same set of equations. Since the flow is supersonic (i.e., $W>a$), all $Z$ derivatives utilize windward first-order differencing. Hence, the values of the potential must be stored at the current and two previous radial or spherical ($Z$) stations.

When the cross flow ($Q_c$) is supersonic, Eq. (12) is rewritten as

$$(a^2-Q_c^2)F_{ss}+a^2F_{nn}-B_1F_{xx}-B_2F_{xy}-B_3F_{yy}$$
$$+(A_4-B_4)F_y+A_5F_x+A_6w+(A_7-B_7)-B_8F_{zz}$$
$$-B_9F_{xz}-B_{10}F_{yz}-B_{11}F_z=0 \tag{13}$$

The general nonconical boundary conditions are defined in Ref. 9. The far field conditions require vanishing of the reduced potential.

## Numerical Formulation, Ring vs Column Relaxation

In Ref. 8, ring relaxation was employed in the cross flow plane iterations (see Fig. 1). The calculation was started at an outer boundary and swept toward the surface of the body. In this technique the symmetry conditions are imposed simultaneously on each ring through periodic end conditions in the tridiagonal matrix. Iterations on the order of the number of radial mesh points are required before the surface boundary condition has propagated out to form the bow shock. Column relaxation, as set forth in this study, inverts the matrix along a mapped cross-sectional radial line ($\theta=$ const) bounded by the surface boundary condition and far field condition of zero reduced potential. Hence, the surface boundary disturbance is immediately propagated at the outer boundary and formation of the bow shock occurs rapidly.

The following numerical formulation is utilized in the column SLOR scheme for the general nonconical equation. The second derivatives, when the cross flow is subsonic (i.e., $Q_c^2=U^2+V^2<a^2$), are approximated by the central difference formulas

$$F_{xx}=\frac{1}{(\Delta x)^2}\left[F_{i+1,j}-\frac{2}{\omega}F^+_{i,j}-2\left(1-\frac{1}{\omega}\right)F_{i,j}+F^+_{i-1,j}\right]$$

$$F_{xy}=\frac{1}{4\Delta x\Delta y}[F_{i+1,j+1}-F^+_{i-1,j+1}-F_{i+1,j-1}+F^+_{i-1,j-1}]$$

$$F_{yy}=\frac{1}{(\Delta y)^2}[F^+_{i,j+1}-2F^+_{i,j}+F^+_{i,j-1}]$$

$$F_{xz}=\frac{1}{2\Delta x\Delta z}[F_{i+1,j}-F^+_{i-1,j}-F^0_{i+1,j}+F^0_{i-1,j}]$$

$$F_{yz}=\frac{1}{2\Delta z\Delta y}[F^+_{i,j+1}-F^+_{i,j-1}-F^0_{i,j+1}+F^0_{i,j-1}] \tag{14}$$

where the + sign denotes new iterate values of the potential, the superscript $0$ denotes known values of the reduced potential at the previous $Z$ station, and the superscript $00$ denotes values at the $Z-2\Delta Z$ station. The subscripts $i$ and $j$ refer to the $X$ and $Y$ directions, respectively. All velocities are determined using previous iterate values of the potential with the exception of the contribution of $F_z$ which is first-order accurate in the marching direction. The total velocity is $Q^2=U^2+V^2+W^2$, where $W$ is the velocity in the radial marching direction ($Z$).

When the cross flow is supersonic, the rotated difference scheme of Ref. 8 is used for the conical terms and the nonconical terms are approximated by windward differences. The best nonconical results were obtained using windward differencing for the nonconical second derivatives in the supersonic cross flow zone. Suitable windward difference formulas are

$$F_{xx}=\frac{1}{(\Delta x)^2}[2F^+_{i,j}-F_{i,j}-2F^+_{i-1,j}+F_{i-2,j}]$$

$$F_{xy}=\frac{1}{\Delta x\Delta y}[F^+_{i-1,j}-2F^+_{i,j}+F_{i,j}+F^+_{i,j+1}-F_{i-1,j+1}]$$

$$F_{yy}=\frac{1}{(\Delta y)^2}[2F^+_{i,j}-F_{i,j}-2F^+_{i,j+1}+F_{i,j+2}]$$

$$F_{xz}=\frac{1}{\Delta x\Delta z}[F^0_{i-1,j}-F^+_{i-1,j}+F^+_{i,j}-F^0_{i,j}]$$

$$F_{yz}=\frac{1}{\Delta y\Delta z}[F^+_{i,j+1}-F^0_{i,j+1}+F^0_{i,j}-F^+_{i,j}] \tag{15}$$

where

$$F_{zz}=\frac{1}{(\Delta z)^2}[F^+_{i,j}-2F^0_{i,j}+F^{00}_{i,j}] \quad \text{for } Q_c^2\gtrless a^2$$

In addition to utilizing the column relaxation, the nonconical terms are no longer treated as forcing functions as in Ref. 9 but are brought into the tridiagonal matrix enhancing the computational efficiency. To ensure stability near the sonic line, an artificial time-like term is added of the form

$$\epsilon F_{St} = \epsilon\left(\frac{V_l}{Q_c} F_{yt} + \frac{U_l}{Q_c} F_{xt}\right)$$

where

$$U_l = \frac{U}{\rho} \qquad V_l = VY_\rho + \frac{U}{\rho} Y_\theta$$

or

$$\epsilon F_{St} = \frac{\epsilon}{Q_c}\left[\frac{V_l}{\Delta y}\left(F^+_{i,j+1} - F^+_{i,j} - F_{i,j+1} + F_{i,j}\right)\right]$$

$$\pm \frac{U_l}{\Delta x}\left(F^+_{i,j} - F^+_{i\mp 1,j} - F_{i,j} + F_{i\mp 1,j}\right) \tag{16}$$

A variable coefficient of the form

$$\epsilon = \frac{K}{|1 - M_c|}$$

where $K$ is a constant and $M_c$ is the cross flow Mach number was found to be most efficient in that the artificial "viscosity" is maximized locally in the vicinity of the sonic line, yet remains continuous throughout both the subsonic and supersonic cross flow regions. A maximum value is imposed for points close to sonic cross flow velocity. This accelerates the computation for cases that would normally require large values of $\epsilon$ for stability.

Figure 2 demonstrates some typical convergence rates on a $30 \times 30$ mesh for both the "ring" and "column" SLOR techniques. Two quite different cases are shown at $M_\infty = 2.0$ and $\theta_c = 20$ deg, a cone at $\alpha = 0$ deg and thin elliptic cone at $\alpha = 10$ deg ($\delta \equiv$ cone centerline angle). For the simple computation of a cone, the convergence rate of the column SLOR technique is 10 times that of the ring relaxation. The thin ellipse, with an embedded supersonic zone and strong cross shock, converged four times faster. Satisfactory convergence for the ellipse occurs at about 50-60 iterations and 15 s on an IBM 3033 machine which is 30% faster than an IBM 370/168.

Obviously, the column relaxation is most efficient for solutions with the least asymmetry. At extreme angles of attack, most probably out of the range of practical computations, the ring and column relaxation schemes should exhibit comparable convergence rates. Hence, for most practical conditions, the column SLOR technique is more suitable and exhibits two to ten times the convergence rate of the ring technique and was adopted for all later computations. The gain in computational efficiency is also carried over into the nonconical flow solutions. The convergence "spikes" shown in Fig. 2 for the ring relaxation technique occur as the bow shock builds up in strength and jumps from one ring location to another. This behavior does not occur in the column relaxation. The computational efficiency of both column and ring SLOR techniques is considerably enhanced using mesh refinement.

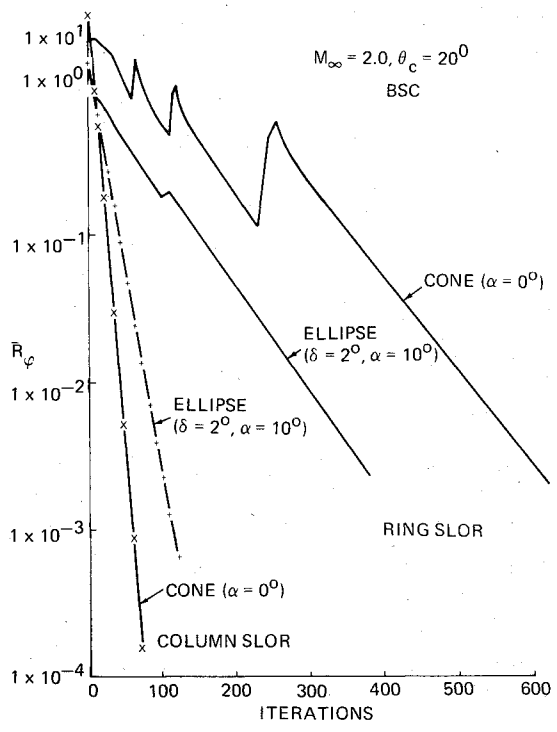


**Fig. 2 Comparison of typical convergence histories for ring vs column SLOR schemes.**

## Conical Shock Fitting

### Isentropic Shock Jump Condition

To fit the bow shock an isentropic jump condition must be imposed at the shock boundary defined as $\rho = c$. Mass continuity is imposed across the shock surface. This condition can be stated simply as

$$\bar{\rho} Q_N = Q_{\infty N}\,|_{\rho = c} \tag{17}$$

where $Q_N$ is the normal velocity to the shock surface and $\bar{\rho}$ is a normalized density given by

$$\bar{\rho} = \left[1 - \left(\frac{\gamma - 1}{2}\right) M^2_\infty (Q^2 - 1)\right]^{\frac{1}{\gamma - 1}} \tag{18}$$

To further derive this condition for general three-dimensional flow in the mapped coordinate frame, let the shock surface be defined as

$$G = \rho - C(\theta, R) \tag{19}$$

The normal velocity of the shock becomes

$$Q_N = \boldsymbol{Q} \cdot \frac{\nabla G}{|\nabla G|} = \left[\frac{\dfrac{V}{RH} - \dfrac{UC_\theta}{CRH} + W\left(h_l - \dfrac{h_2 C_\theta}{C} - C_R\right)}{|\Delta G|}\right] \tag{20}$$

Substituting Eq. (20) into the shock condition Eq. (17) leads to

$$\bar{\rho}_s\left[V_s - \frac{U_s C_\theta}{C} + W_s RH\left(h_l - C_R - \frac{h_2 C_\theta}{C}\right)\right]$$

$$= v_\infty - \frac{u_\infty C_\theta}{C} + w_\infty RH\left(\frac{h_l - h_2 C_\theta - C_R}{C}\right) \tag{21}$$

where the subscript $s$ denotes properties of the high-pressure side of the shock. Equation (21) is the general three-dimensional isentropic shock jump condition which, for conical flow, reduces to

$$\bar{\rho}_s (CV_s - U_s C_\theta) = Cv_\infty - u_\infty C_\theta \tag{22}$$

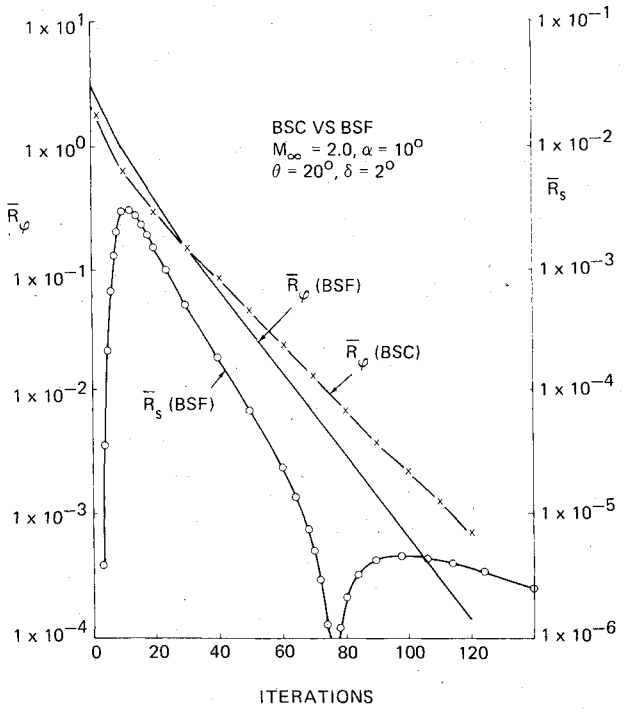


**Fig. 3 A comparison of convergence histories for bow shock fit vs bow shock capture solutions for a subsonic leading-edge elliptic cone.**

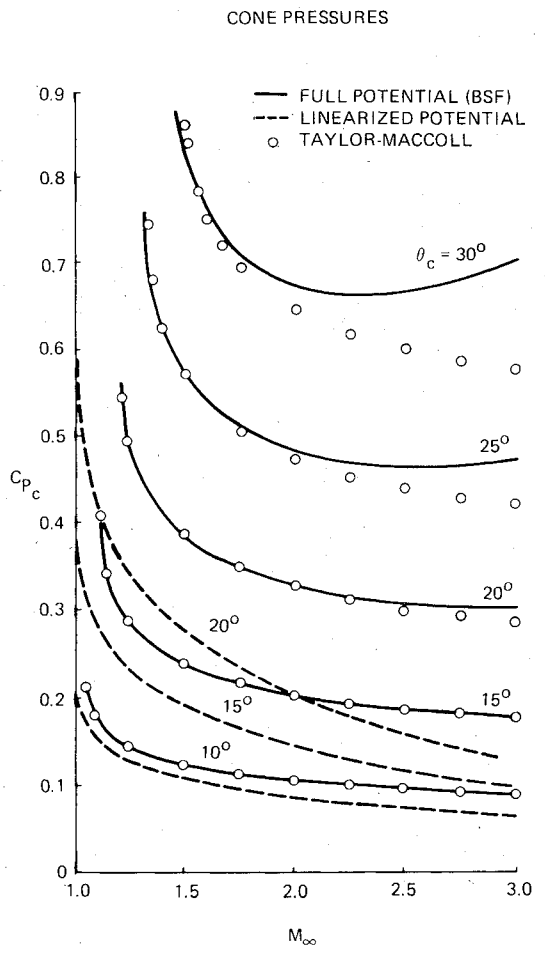


**Fig. 4 A comparison between Taylor-Maccoll, full potential (BSF) and linearized potential solutions for cone surface pressure coefficients vs freestream Mach number.**

Equation (21) or (22) must be satisfied at each shock point boundary. The reduced potential is identically zero at the shock boundary which satisfies the momentum equation tangent to the shock wave. The flow tangent to the shock is then just given by the freestream conditions.

Hence, at $\rho = C$, $F = 0$ and Eq. (21) or (22) must be solved to determine the shock surface. The derivative along the shock surface ($F_x$) is identically zero. The derivative in the cross flow radial direction ($Y$) at the shock surface is computed using a one sided second-order differencing of the interior flow points. For conical flow, Eq. (22) can be written in tridiagonal difference form as

$$-\frac{\tilde{\rho}_s U_s C^+_{i+1}}{2\Delta\theta} + \tilde{\rho}_s V_s C^+_i + \frac{\tilde{\rho}_s U_s C^+_{i-1}}{2\Delta\theta} = Cv_\infty - u_\infty C_\theta \qquad (23)$$

The right-hand side of Eq. (23) is written using old values of the shock surface as a forcing function. For subsonic leading-edge geometries the shock surface initially is set as the rotated Mach cone. After one complete sweep in the cross flow plane, Eq. (23) is inverted to determine the new shock shape. The new shock shape is under-relaxed. The shock convergence inherently lags behind the interior flow points. The under-relaxation is also necessary to avoid the occurrence of supersonic cross flow points inside the shock surface, that is, to avoid shock capture. Since the bow shock is a boundary, the entire mesh must be recomputed after determining a new shock surface. Hence, the mesh is changing continually with the iterative scheme. Convergence is achieved when the residuals at interior points and the residual associated with the shock jump condition are reduced to a specified tolerance. Equation (23) was found to be a suitable implicit recursive formula to obtain shock convergence. No attempts were made to further optimize the shock scheme in terms of computational efficiency.

Figure 3 shows a typical convergence history for a BSF subsonic leading-edge elliptic cone vs the BSC case. Some additional gain in convergence rate is achieved with the BSF method. The shock residual is initially zero for the rotated Mach cone and zero potential field. As the shock strength builds, the shock residual reaches a maximum value and then declines with further iterations. The BSF method requires fewer radial points in the cross-flow plane than the BSC method since in the BSC the shock location is not known a priori, and an outer boundary must be set far enough to allow capture; hence, wasting points of freestream conditions beyond the actual shock boundary. Unfortunately, the gain in convergence rate and mesh points in the BSF method is offset by the additional work required to recompute the mesh metrics and derivatives for each cycle. Typically, subsonic leading edge BSF solutions take two to three times the work of a BSC method with column SLOR.

The characteristics of the shock residual convergence history is largely dependent upon the relaxation factor. For the results in Fig. 3, an under-relaxation factor of 0.75 was used. The secondary rise in the average shock residual occurs when the maximum residual comes from the leeward shock point. The leeward shock point should lie on the Mach cone at this angle of attack (i.e., zero strength shock). Evidently, a slight overshoot of this position has occurred as indicated by the slight rise in shock residual. A slightly lower relaxation factor should eliminate this occurrence.

Evaluation of the accuracy of the full potential BSF solutions was investigated for cones at zero angle of attack. Figure 4 shows a plot of surface pressure coefficients for cones of various half angles vs freestream Mach number. Also plotted are Euler or Taylor-Maccoll solutions and linearized potential results.

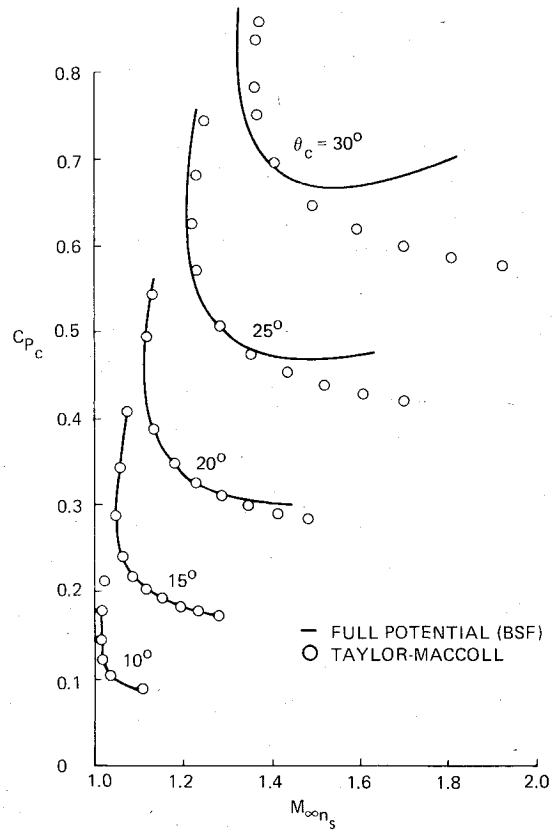


**Fig. 5 A comparison between Taylor-Maccoll and full potential (BSF) for cone surface pressure coefficients vs the normal freestream Mach number at the shock.**

Excellent agreement between Euler and full potential BSF pressures are obtained for Mach numbers up to 3 and cone angles below 20 deg. Above 20 deg, the two solutions begin to depart at a lower Mach number. The linearized potential solution degrades dramatically beyond 10-deg cones. Figure 5 shows a plot of cone surface pressure coefficients vs the normal freestream Mach number at the shock given by the full potential and Euler solutions. Generally good agreement is obtained up to a normal freestream Mach number of 1.4. An interesting aspect of these curves is that the two solutions also depart slightly at the larger cone angles where the cone contains a significant region of subsonic flow. In this region, even though the surface pressure shows agreement, the shock angles predicted by the full potential solution are less than the Euler solutions. Hence, solving the full potential equation significantly advances the accuracy of the solution over the linearized potential. For thin wings of 55-60 deg sweep angles, the full potential should yield accurate results because the normal Mach number at the shock decreases rapidly as a function of cross-sectional axis ratio (e.g., $\theta_c/\delta$).

Figure 6 shows a comparison between the BSF and BSC methods for a thin elliptic cone with a subsonic leading edge ($\theta_c = 20$ deg) at $M_\infty = 2.0$ and several angles of attack. In all of the comparisons to follow, a (58 × 58) mesh is used for both bow shock fit and captured solutions with mesh refinement. Excellent agreement in surface pressures are obtained with the bow shocks also showing good agreement with a slight departure at the highest angle of attack. Figure 7 shows another set of comparisons at $M_\infty = 2$, $\alpha = 10$ deg for three thin elliptic cones with subsonic, sonic, and supersonic leading edges. The sonic and supersonic leading-edge cones required an initial guess other than the rotated Mach cone for the initial shock surface with care taken not to define an initial surface outside the true bow shock (i.e., leading-edge modifications in the rotated Mach cone shape). The leeward surface pressures show excellent agreement. The windward

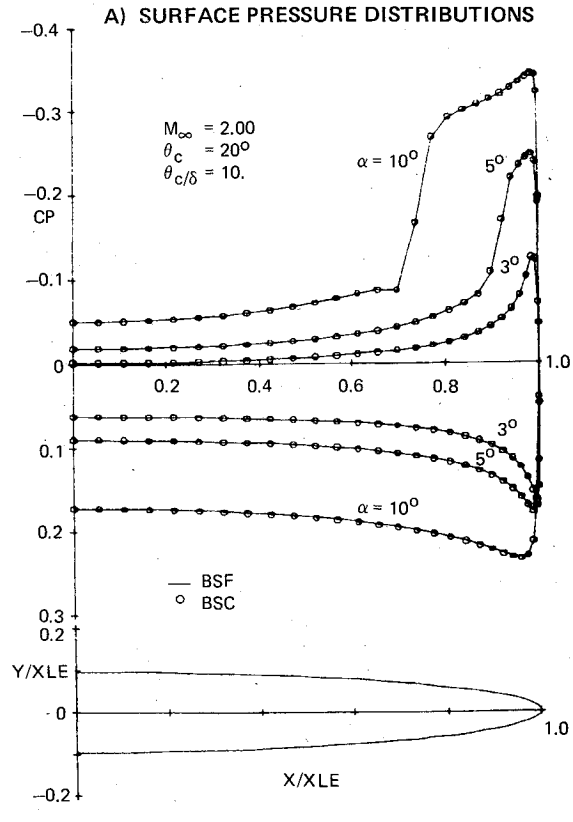


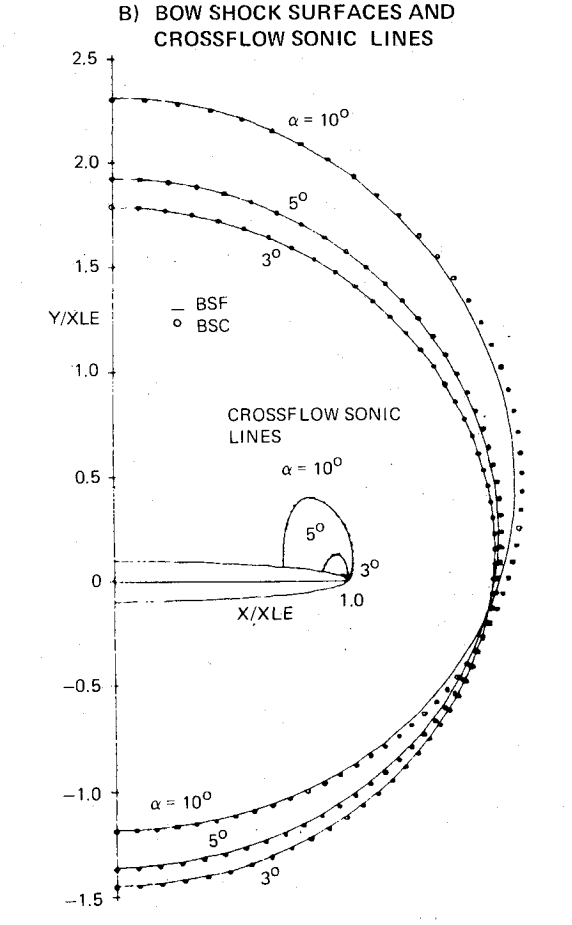


**Fig. 6 A comparison of full potential conical solutions, BSF vs BSC, for an elliptic subsonic leading-edge cone ($\theta_c = 20$ deg, $\theta_c/\delta = 10$) at $M_\infty = 2.00$, $\alpha = 3$, 5, and 10 deg.**

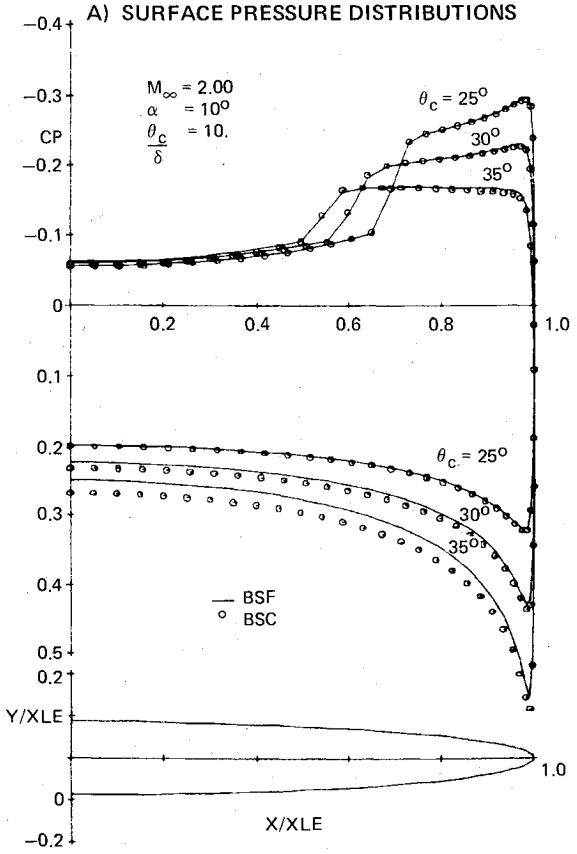


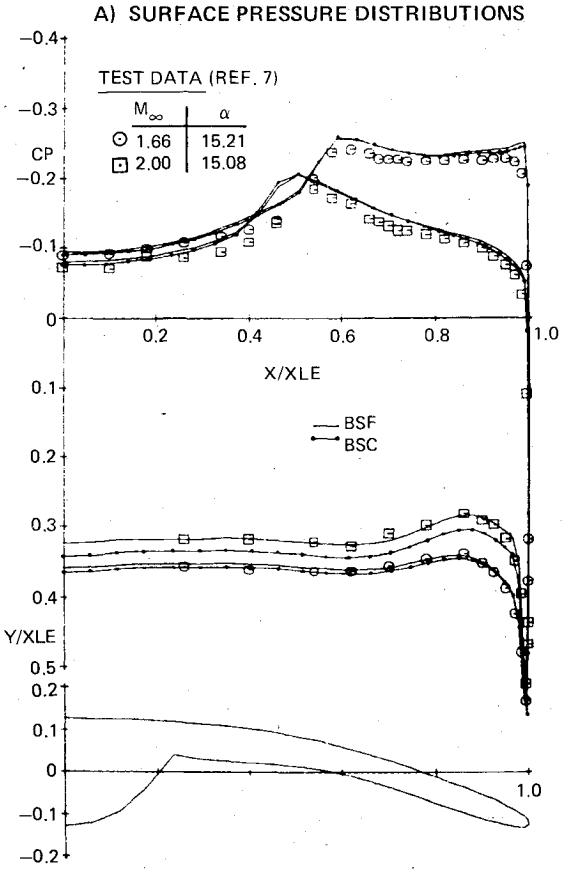


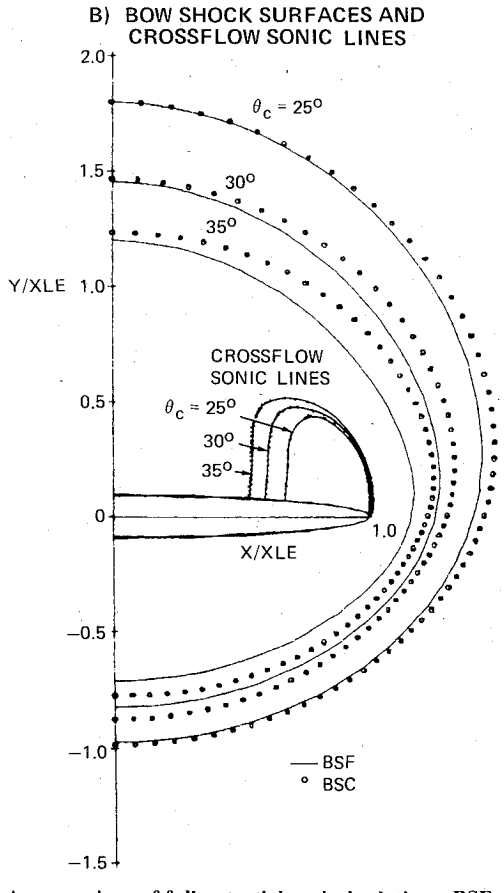


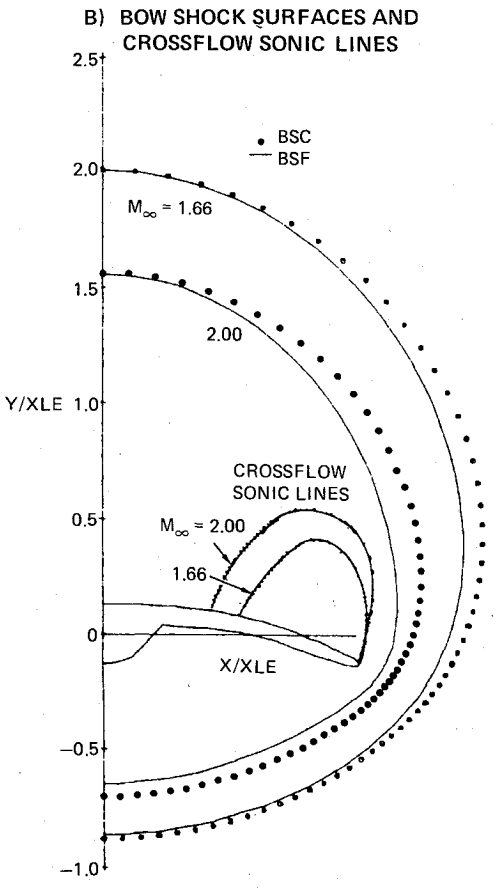


Fig. 7 A comparison of full potential conical solutions, BSF vs BSC, for various elliptic cone leading edges (subsonic, sonic, and supersonic) at $M_\infty = 2.00$, $\alpha = 10$ deg, and $\theta_c/\delta = 10.0$.

Fig. 8 A comparison of full potential solutions, BSF vs BSC, with experiment of surface pressure data for a conically cambered wing with a centerbody.

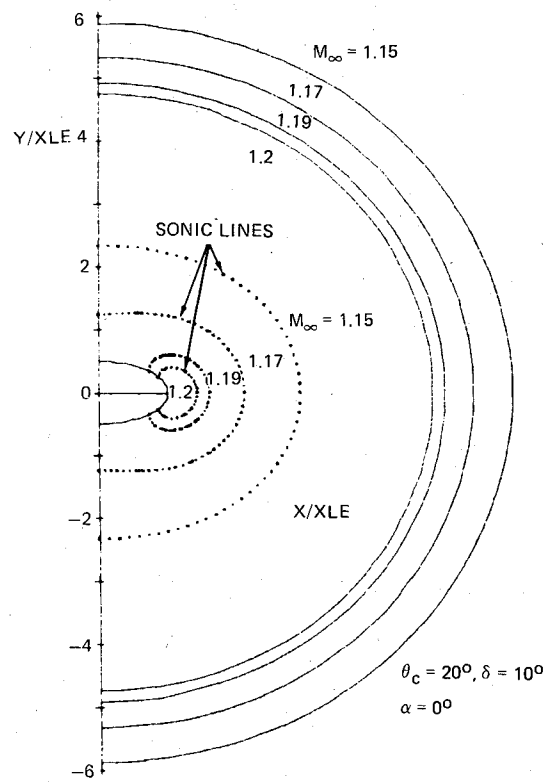


**Fig. 9 Conical (BSF) solutions with embedded subsonic regions for an elliptic cone ($\theta_c = 20$ deg, $\delta = 10$ deg) at zero angle of attack and Mach numbers 1.20, 1.19, 1.17, and 1.15.**

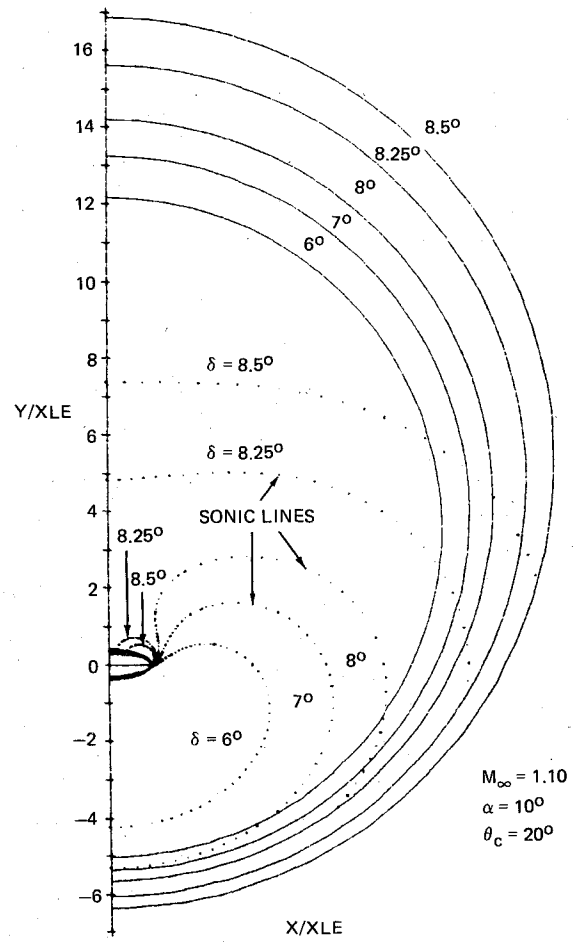


**Fig. 10 Conical (BSF) solutions with embedded subsonic regions at $M_\infty = 1.10$, $\alpha = 10$ deg for various elliptic cones $\theta_c = 20$ deg, and $\delta = 6$, 7, 8, 8.25, and 8.50 deg.**

surface pressures begin to depart at the sonic leading-edge wing with increasing discrepancy for the supersonic leading-edge cone. Figure 7b shows a comparison of the computed shock shapes. The BSC surfaces all lie upstream of the BSF solution. This is consistent with the transonic conservative vs nonconservative observations in that the conservative BSF solutions lie downstream of the nonconservative BSC solutions. It should be mentioned that the bow shock shape from the capture solutions are obtained by interpolation for the outer cross flow sonic line.

Figure 8 shows further a comparison of predicted surface pressures with experimental data for the conical cambered wing of Ref. 7. For a slightly subsonic leading-edge solution at $M_\infty = 1.66$, $\alpha = 15.21$ deg, both the BSC and BSF solutions show excellent agreement with the test data. For $M_\infty = 2.00$, $\alpha = 15.08$ deg, corresponding to a supersonic leading-edge case, the BSF solution shows excellent agreement for the windward surface pressures whereas the BSC solution overpredicts these pressures. Both solutions yield comparable results for the leeward pressures showing some discrepancy in the location and strength of the embedded shock either due to boundary-layer or nonconservative effects. These trends agree with those obtained previously, namely, the BSC solutions are very accurate for the condition of subsonic leading edge and tend to slightly overpredict the windward pressures for stronger shock conditions (i.e., supersonic leading edges).

### Conical Solutions with Embedded Regions of Total Subsonic Mach Number

As an interesting aside and a preliminary demonstration of the general applicability of the present technique in handling regions of three-dimensional subsonic flows, conical solutions having embedded subsonic regions were generated.

Figure 9 shows a series of such solutions in the freestream Mach number range of 1.15-1.20 for a 20-deg elliptic cone at zero angle of attack. At a Mach number of 1.20, a small region of subsonic flow is formed in the vicinity of the leading edge terminating on the cone surface. As the Mach number is decreased, the subsonic region gets larger, and lifts off the cone, terminating at the symmetry planes.

Figure 10 shows another series of solutions at Mach number 1.10 and $\alpha = 10$ deg for a 20-deg elliptic cone. The centerline angle ($\delta$) of the elliptic cone was varied from 6 to 8.5 deg. At a centerline angle of 6 deg, an isolated pocket of subsonic flow occurs on the windward side of the cone. At 7 deg, the sonic line intersects the bow shock indicating that all of the flow in the vicinity of the windward symmetry plane between the body and bow shock is subsonic. Further increase in the centerline angle causes the sonic line to extend into the leeward flow. An interesting feature of these solutions is that a small region of supersonic flow persists in the vicinity of the leeward leading edge cone surface at the centerline angles of 8.25 and 8.50 deg. Two distinct sonic lines are formed, a leading-edge sonic line terminating at the cone surface and another sonic line extending from the bow shock to the leeward symmetry plane. Although not shown, solutions were found to exist which contained both a subsonic total Mach number region and a supersonic cross flow Mach number region and, hence, an embedded cross flow shock.

## Conclusions

A column SLOR scheme with shock capturing was found to be two to ten times more computationally efficient than the ring SLOR scheme of Ref. 8 for most supersonic conical flows of practical interest. This efficiency is also carried over into three-dimensional calculations.

A new fully implicit isentropic bow shock fitting technique has been demonstrated on a variety of conical flow solutions and compared to shock captured solutions for the non-conservative full potential equation. Excellent agreement between the BSC and BSF conical solutions was obtained for subsonic leading-edge solutions. The BSC solution has a tendency to overpredict the windward surface pressures for stronger shock conditions such as supersonic leading edges and yields a shock position upstream of the conservative BSF solution in agreement with transonic flow observations. The windward pressure predicted by the BSF method was validated by experimental data. The two solutions yield virtually identical results for the leeward behavior.

## Acknowledgment

The author wishes to thank Dr. F. Marconi of the Research Department, Grumman Aerospace Corporation, for the helpful discussions and suggestions made in regard to shock fitting.

## References

[1] Brown, C., McLean, F., and Klunker, E., "Theoretical and Experimental Studies of Cambered and Twisted Wings Optimized for Flight at Supersonic Speeds," *Proceedings of the 2nd International Congress of Aeronautical Sciences, Advances in Aeronautical Science*, Vol. 3, edited by T. von Kármán et al., Pergamon Press, Oxford, 1962.

[2] Marconi, F., Salas, M., and Yeager, L., "Development of a Computer Code for Calculating the Steady Super/Hypersonic Inviscid Flow Around Real Configurations, Vol. I—Computational Techniques," NASA CR 2675, April 1976.

[3] Kutler, P., "Computation of Three-Dimensional Inviscid Supersonic Flows," *Progress in Numerical Fluid Dynamics, Lecture Notes in Physics*, Vol. 41, Springer-Verlag, Berlin, 1975, pp. 287-374.

[4] Marconi, F. and Siclari, M. J., "A Study of the Inviscid Flow about Conically Cambered Delta Wings," AIAA Paper 78-58, Jan. 1978.

[5] Siclari, M. J., "Investigation of Cross Flow Shocks on Delta Wings in Supersonic Flow," *AIAA Journal*, Vol. 18, Jan. 1980, pp. 85-93.

[6] Mason, W. H. and DaForno, G., "Opportunities for Supersonic Performance Gains Through Non-Linear Aerodynamics," AIAA Paper 79-1527, July 1979.

[7] Mason, W. H. and Miller, D. S., "Controlled Supercritical Crossflow on Supersonic Wings—An Experimental Validation," AIAA Paper 80-1421, 1980.

[8] Grossman, B., "Numerical Procedure for the Computation of Irrotational Conical Flows," *AIAA Journal*, Vol. 17, Aug. 1979, pp. 828-837.

[9] Grossman, B. and Siclari, M. J., "Nonlinear Supersonic Potential Flow over Delta Wings," *AIAA Journal*, Vol. 19, May 1981, pp. 573-581.

[10] Jameson, A., "Iterative Solution of Transonic Flow over Airfoils and Wings, Including Flows at Mach 1," *Communications on Pure and Applied Mathematics*, Vol. 27, May 1974, pp. 283-309.

[11] Siclari, M. J., Marconi, F., and Grossman, B., "Analysis and Design of Supersonic Aircraft based on Inviscid Nonlinear Eulerian Equations," AFWAL TR-80-3110, Pts. I and II, Oct. 1980.